

Enhanced Photoelectrochemical Performance from Rationally Designed Anatase/Rutile TiO₂ Heterostructures

Fengren Cao,^{†,||} Jie Xiong,^{§,||} Fangli Wu,[†] Qiong Liu,[†] Zhiwei Shi,[†] Yanhao Yu,[‡] Xudong Wang,^{*,‡} and Liang Li^{*,†}

[†]College of Physics, Optoelectronics and Energy, Center for Energy Conversion Materials & Physics (CECMP), Jiangsu Key Laboratory of Thin Films, Soochow University, Suzhou 215006, People's Republic of China

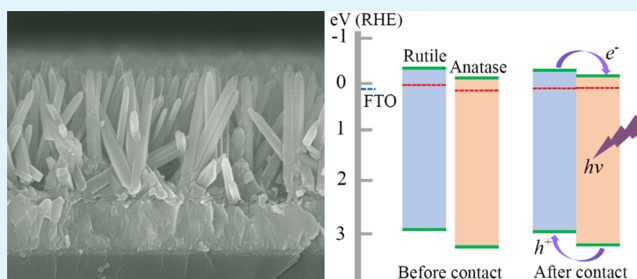
[‡]Department of Materials Science and Engineering, University of Wisconsin—Madison, Madison, Wisconsin 53706, United States

[§]State Key Laboratory of Electronic Thin Films and Integrated Devices, University of Electronic Science and Technology of China, Chengdu 610054, People's Republic of China

S Supporting Information

ABSTRACT: In a photoelectrochemical (PEC) cell for water splitting, the critical issue is charge separation and transport, which is usually completed by designing semiconductor heterojunctions. TiO₂ anatase–rutile mixed junctions could largely improve photocatalytic properties, but impairs PEC water splitting performance. We designed and prepared two types of TiO₂ heterostructures with the anatase thin film and rutile nanowire phases organized in different sequences. The two types of heterostructures were used as PEC photoanodes for water splitting and demonstrated completely opposite results. Rutile nanowires on anatase film demonstrated enhanced photocurrent density and onset potential, whereas strong negative performance was obtained from anatase film on rutile nanowire structures. The mechanism was investigated by photoresponse, light absorption and reflectance, and electrochemical impedance spectra. This work revealed the significant role of phase sequence in performance gain of anatase–rutile TiO₂ heterostructured PEC photoanodes.

KEYWORDS: TiO₂, photoelectrochemical, atomic layer deposition, heterostructure, water splitting



INTRODUCTION

Photoelectrochemical (PEC) water splitting for H₂ production has been regarded as a promising strategy to resolve the energy and environment crisis.^{1–5} Fundamentally, PEC water splitting includes three steps: exciton generation from photon absorption, electron–hole pair separation, and electrochemical reaction at the semiconductor/electrolyte interface. These three processes are correspondingly determined by light-harvesting capability, charge separation efficiency, and surface reaction kinetics. Among them, charge separation efficiency can be enhanced by designing heterojunctions with favorable built-in potential distribution.^{6–12} Recently, a new type of heterojunction, called a mixed junction formed by two different phases of one semiconductor, was found to be effective in driving the electron and hole toward the desired direction.^{13–17} This discovery provides a new path to enhancing the charge separation and performing efficient water splitting.

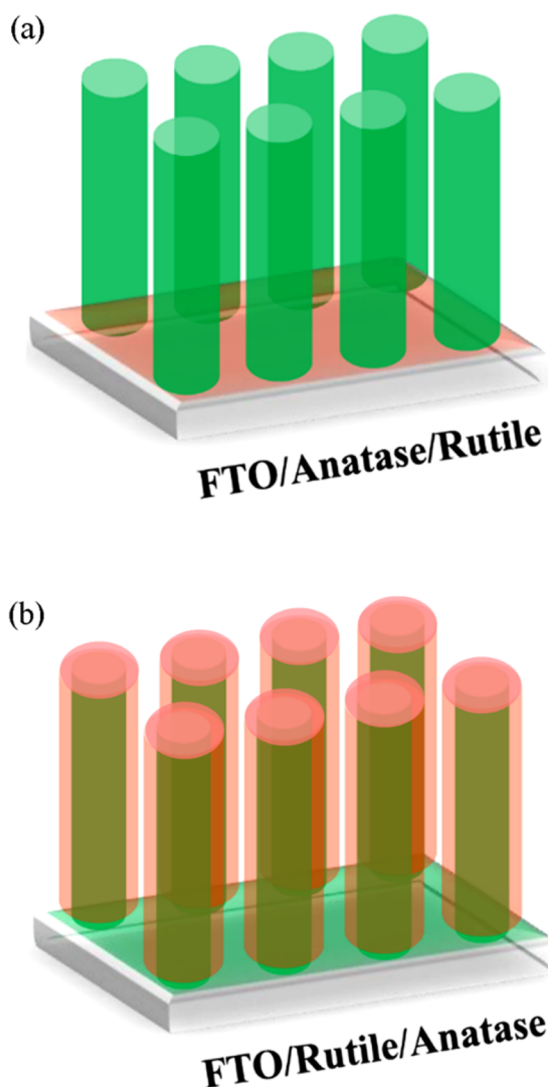
Titanium dioxide (TiO₂) is one of the most promising photocatalytic (PC) and PEC materials owing to the favorable conduction band edge, good stability, and low cost.¹⁸ Compared with single anatase or rutile phase TiO₂, anatase–rutile mixed TiO₂ is found to be capable of substantially improving the PC performance by facilitating the charge separation and prolonging the carrier lifetime.^{13,19,20} However,

the underlying mechanisms (e.g., charge transfer direction across the heterojunction) in these PC systems remain unclear because PC reactions are commonly sensitive to a number of variations other than the heterojunction, such as material qualities and measurement techniques.^{21,22} On the other hand, PEC systems are typically well controlled and precisely monitored, providing an ideal platform for study of the mechanism.^{23–25} Therefore, introducing an anatase–rutile TiO₂ heterojunction to the PEC system is expected to not only accomplish remarkable performance gain but also clear the charge transfer scenario. Nevertheless, to date, few investigations are devoted to studying the effect of mixed-phase junctions on PEC water splitting. In this paper, the influence of the anatase–rutile TiO₂ heterojunction on the charge separation and PEC performance was systematically studied. As shown in Scheme 1, two types of anatase–rutile TiO₂ heterojunctions (i.e., FTO/anatase/rutile and FTO/rutile/anatase) were developed by hydrothermally growing rutile TiO₂ nanorods and atomic layer deposition of anatase TiO₂ film. The photogenerated electrons were found to be eager to

Received: March 31, 2016

Accepted: May 3, 2016

Published: May 3, 2016

Scheme 1. Schematic View of (a) Anatase/Rutile and (b) Rutile/Anatase Junctions on FTO Substrates^a

^aThe red and green colors represent the anatase and rutile TiO₂, respectively.

transfer from the rutile to the anatase phase, and photo-generated holes had a high tendency to migrate from anatase to rutile. As a result, the FTO/anatase/rutile TiO₂ photoanode exhibited considerable PEC performance improvement compared with the FTO/rutile TiO₂ structure. In contrast, the FTO/rutile/anatase photoanode showed significant performance reduction, and the efficiency loss enlarged with the increase of anatase film thickness. These results can be a valuable guide for designing efficient phase heterojunctions for improved PEC properties.

RESULTS AND DISCUSSION

TiO₂ nanorod arrays are grown on FTO substrates by the hydrothermal method. Figure 1 shows top (a) and (b) cross-sectional view SEM images of pristine TiO₂ nanorod arrays that were directly grown on FTO substrates (defined as pristine). The nanorods are tetragonal in shape and quasi-vertically standing on the substrate with an identical length. The average diameter of rutile nanowires is about 150 nm. The tetragonal shape is consistent with the growth habit of rutile TiO₂.^{26,27} To

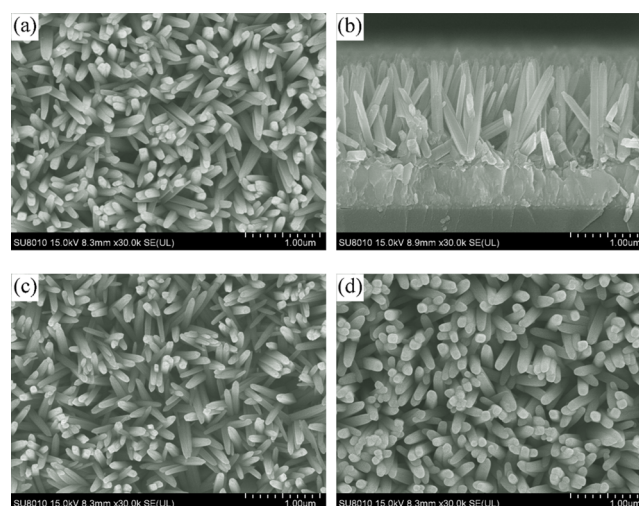


Figure 1. SEM images of samples: (a) top and (b) cross-sectional views of pristine TiO₂ nanorod arrays grown directly on FTO substrates (pristine); (c) nanorod arrays grown on FTO substrates using 20 nm ALD TiO₂ films as seeding layers (20AR); (d) nanorod arrays coated with 20 nm ALD TiO₂ films after the direct growth on FTO substrates (20RA).

fabricate the FTO/anatase/rutile TiO₂ structure, 5, 10, and 20 nm thicknesses of TiO₂ films are deposited onto the FTO substrates by atomic layer deposition (ALD) before the hydrothermal growth of rutile TiO₂ nanorods (labeled SAR, 10AR and 20AR, where A, R, and the number correspond to anatase films, rutile nanorods, and anatase film thickness, respectively). The diameter, length, and density of the rutile TiO₂ nanorods with the anatase film are similar to those of the pristine case (Figure 1c; Figures S1 and S2). The FTO/rutile/anatase TiO₂ structures are constructed by coating the pristine nanorods using different thicknesses (5–20 nm) of ALD TiO₂ films (labeled 5RA, 10RA, and 20RA, where R, A, and the number are the same as those above). With the increase of the ALD film thickness, the diameters of rutile nanorod increase gradually (Figure 1d; Figure S3), indicating the formation of core/shell nanorod arrays. Particularly, the surfaces of 20 nm film coated nanorods became obviously round. Low-magnification SEM images (Figures S4 and S5) present the uniform growth of large-scale nanorod arrays.

Figure 2 shows the X-ray diffraction (XRD) patterns and Raman spectra of the pristine, AR, and RA samples. Figure 2a compares the XRD patterns of FTO substrate, pristine, and 5RA–20RA. The pristine shows a single rutile phase with the 101 peak beside the FTO peaks. The anatase TiO₂ peak with a primarily 101 orientation is observed for the 10RA and 20RA samples, suggesting the formation of rutile TiO₂ nanorods coated with ALD anatase TiO₂ films. For the AR samples, the thin ALD films are underneath long nanorods, and X-ray is difficult to collect diffraction signal, as shown in Figure S6, and thus we directly measure ALD films to confirm the corresponding phase. The XRD patterns of ALD anatase TiO₂ films (5–20 nm) on FTO substrate exhibit only the diffraction of FTO, and no TiO₂ peaks are identified (Figure 2b), due to the thin film thicknesses. Phase structures of 5 nm TiO₂ films on FTO substrates are further measured by Raman spectra, as shown in Figure 2c. The vibrational modes at 145, 395, 516, and 637 cm⁻¹ exhibit the characteristic Raman bands of single anatase phase. The rutile TiO₂ is also confirmed by

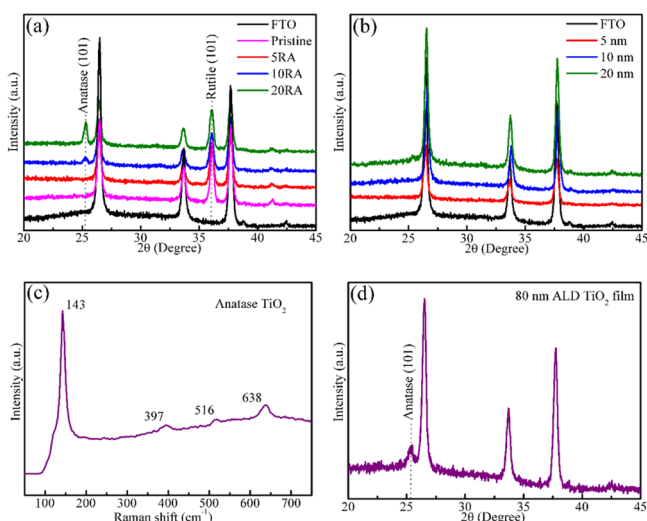


Figure 2. XRD patterns of (a) SRA-20RA and (b) different thicknesses of ALD TiO₂ films on FTO substrates; (c) Raman spectrum of 5 nm thick ALD TiO₂ films; (d) XRD pattern of 80 nm thick ALD TiO₂ films.

Raman spectrum (Figure S7). To obtain XRD diffraction peaks of anatase TiO₂, we deposit thicker ALD TiO₂ film up to 80 nm, and the typical 101 peak of pure anatase phase appears (Figure 2d).

The morphology and microstructure of AR and RA samples are further characterized by transmission electron microscopy (TEM) and high-resolution TEM (HRTEM) images. Figure 3

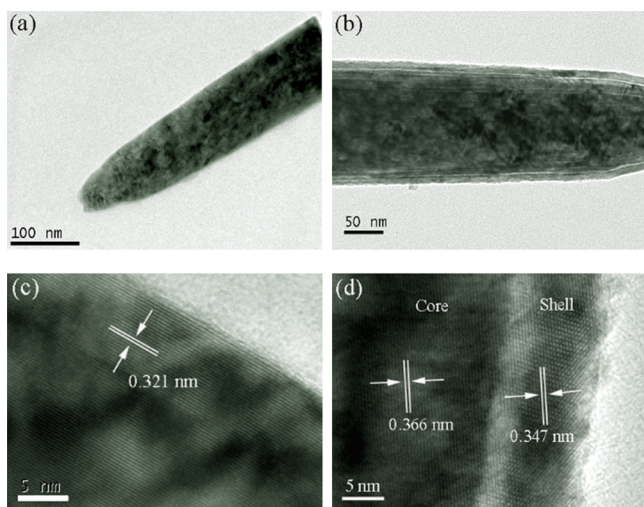


Figure 3. TEM and corresponding HRTEM images of (a, c) 10AR and (b, d) 10RA.

includes TEM and HRTEM images of TiO₂ nanorods scratched from 10AR and 10RA. For the 10AR, we did not obtain the TEM sample of nanorods with ALD film, because the film is very thin and the layer-by-layer growth mechanism of ALD makes the film closely adhere onto the FTO substrate. The lattice fringes correspond to the (110) plane of rutile TiO₂, and the sharp surface indicates no apparent disorder layer. For the 10RA, it can be seen that 10 nm thick TiO₂ film densely and uniformly covers the whole surface of 10RA. The HRTEM result shows that TiO₂ nanorods (core region) are single crystalline rutile phase with the (100) exposed planes (lattice

spacing is 0.366 nm). The ALD TiO₂ films (shell region) have clear lattice fringes with interplanar spacing of 0.347 nm, corresponding to the (101) planes of the anatase phase. The TEM images of 5RA and 20RA are shown in Figure S8. These XRD, Raman, and TEM results confirm the successful fabrication of the anatase film/rutile nanorod (AR) and rutile nanorod/anatase film (RA) heterostructures.

The light absorption and reflectance properties of RA and AR samples were investigated by a UV-vis spectrophotometer with an integration sphere (Figure 4). As a result of the similar

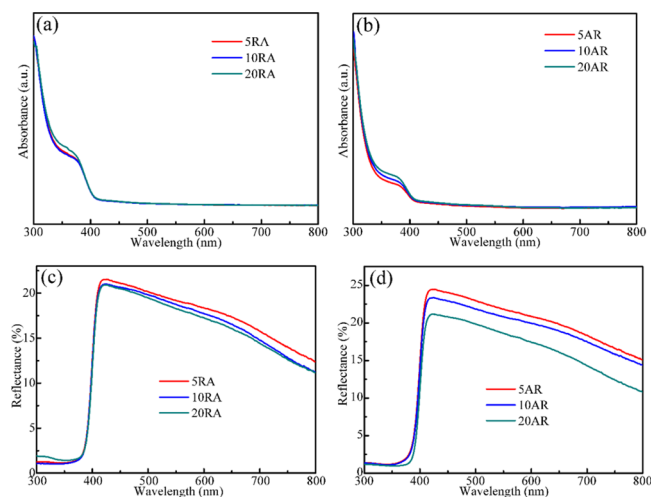


Figure 4. Absorption spectra of (a) SRA-20RA and (b) SAR-20AR; reflectance spectra of (c) SRA-20RA and (d) SAR-20AR.

band gap of anatase and rutile TiO₂, the absorption edges of all samples are located at about 400 nm and the absolute absorption values are almost identical (Figure 4a,b). To obtain the exact band gap, the absorption spectra of anatase film and rutile nanorod array are measured. The relationship between the incident photon energy and the absorption coefficient is plotted in Figure S9 following the equation

$$(\alpha h\nu)^2 = A(h\nu - E_g)$$

where α is the absorption coefficient, h is the Planck constant, ν is the photon frequency, A is a constant, and E_g is the band gap. The band gap of anatase and rutile TiO₂ is calculated to be 3.31 and 3.08 eV, respectively. The reflectance spectra (Figure 4c,d) show that the reflectance values of both ARs and RAs decrease when increasing the thicknesses of anatase films. Decreased reflectance usually leads to better light-harvesting capability, producing increased photocurrent density. Here, an opposite trend is found in $J-V$ curves for all samples (Figure 5), indicating that the optical behaviors cannot govern the performance of PEC water splitting.

The PEC performance of AR and RA heterostructures is then evaluated in 0.1 M KOH solution. The potential is converted to the reversible hydrogen electrode (RHE) potential based on the Nernst equation^{28–31}

$$E_{\text{RHE}} = E_{\text{Ag/AgCl}} + 0.059\text{pH} + E_{\text{Ag/AgCl}}^{\circ}$$

where E_{RHE} is the converted potential versus RHE, $E_{\text{Ag/AgCl}}$ is the measured potential versus the Ag/AgCl reference electrode, and $E_{\text{Ag/AgCl}}^{\circ} = 0.1976$ V at 25 °C. The current density versus potential ($J-V$) curves under simulated solar illumination (100 mW cm⁻²) are illustrated in Figure 5a,b. Compared with the

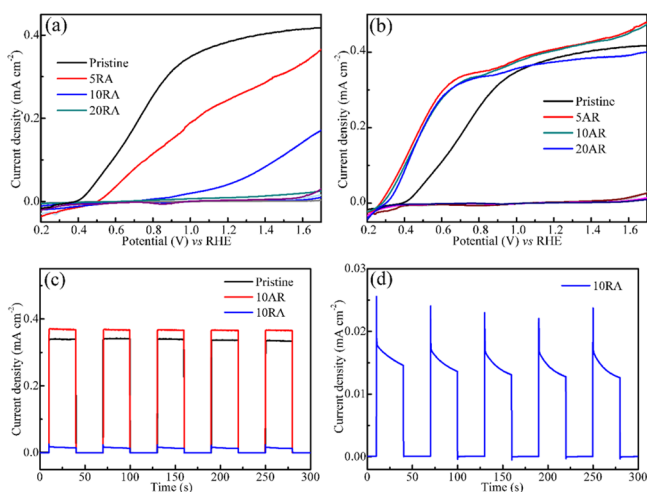


Figure 5. Photocurrent-applied potential curves: (a) pristine and SRA–20RA, (b) pristine and 5AR–20AR; (c) time-dependent photocurrent tests for pristine, 10AR, and 10RA; (d) enlarged figure for 10RA.

pristine, the RAs have three features (Figure 5a). First, upon sweeping the potential, a lower photoresponse is observed in the whole potential range. When the thickness of the anatase film increases from 5 to 20 nm, the photocurrent density decreases hugely. At 1.0 V, the pristine has the highest current value of 0.35 mA cm^{-2} , followed by 0.19 mA cm^{-2} (SRA), 0.02 mA cm^{-2} (10RA), and 0.008 mA cm^{-2} (20RA). Second, in the high bias region, the pristine possesses a saturated photocurrent density, whereas the RAs have continuously increasing value with the increased potential. This observation indicates the charge transport property of pristine photoanode is better than the RA case. Third, the onset potentials of pristine, SRA, 10RA, and 20RA are 0.38, 0.5, 0.68, and 0.75 V vs RHE, respectively. The positive shift of onset potential caused by the anatase TiO_2 coating means higher external voltages are required to drive water splitting in the RA samples.

In the case of ARs (Figure 5b), at the same applied bias, the photocurrent densities of 5AR and 10AR are higher than that of the pristine over the entire potential range. Compared with pristine, 20AR has a higher photocurrent density in the low bias region, but a lower current density in the high bias region, implying 5–10 nm is the optimum thickness. The photocurrent density gradually increases with decreased thickness of ALD anatase TiO_2 films. In comparison with the onset potential of pristine (0.38 V), the ARs shift negatively to 0.30, 0.28, and 0.27 V as the thickness of the anatase TiO_2 films decreases from 20 to 10 and 5 nm. The increased photocurrent density and the negatively shifted onset potential indicate that PEC efficiency of TiO_2 photoelectrode can be improved by introducing the AR heterostructures.

It is well-known that the onset potential and photocurrent are seriously affected by charge separation and recombination processes; thus, we measure the transient $J-t$ curves at 1.0 V bias vs RHE (Figure 5c). A higher photocurrent density is generated in the 10AR. The fast and steady production/extinction upon light on/off indicate efficient charge separation and low recombination in the AR electrode. For 10RA, the photocurrent density is too low to be distinguished, so its $J-t$ curve is plotted separately as Figure 5d. The negligible value of photocurrent density compared to the dark current implies a small concentration of photogenerated holes that involved into

the oxygen evolution reaction. An initial current spike is followed by an exponential decrease from about 0.023 to 0.013 mA cm^{-2} within 30 s. This phenomenon suggests a fast recombination process in RA structures. These results show a convincing conclusion that FTO/anatase/rutile junctions improve PEC performances by increasing the photocurrent density and decreasing the onset potential. Conversely, FTO/rutile/anatase junctions are extremely unfavorable structures for PEC water splitting. The long-term measurements show that both AR and RA heterojunctions have a fairly stable photoresponse (Figure S10).

To further elucidate the relationship between the heterojunctions and the improved water splitting, electrochemical impedance (EIS) measurements are carried out,^{32–34} from which the capacitances are derived and the Mott–Schottky (M–S) plots are generated (Figure 6). The flat band potential

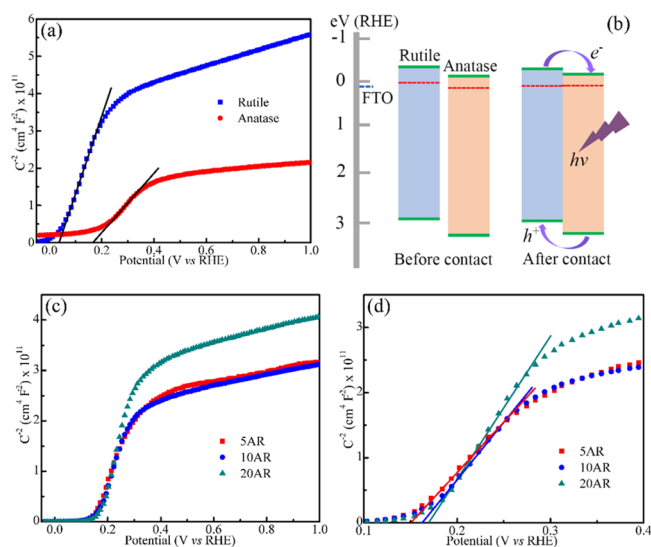


Figure 6. (a) M–S plots of pristine rutile nanorods and anatase films; (b) schematic diagram showing the approximate energy band diagram of the anatase–rutile junctions before and after contact; (c) M–S plots of 5AR–20AR junctions; (d) corresponding zoomed M–S curves.

and carrier density at the electrode/electrolyte interface can be estimated by the M–S equation^{35–38}

$$1/C^2 = (2/e\epsilon\epsilon_0 N_d)[(V - V_{FB} - kT/e)]$$

where C is the capacitance of the space charge region, e is the electron charge, ϵ is the dielectric constant of the semiconductor ($\epsilon_{\text{rutile}} = 170$),³⁹ ϵ_0 is the permittivity of the free space, N_d is the donor density, V is the applied potential, V_{FB} is the flat band potential, k is the Boltzmann constant, and T is the absolute temperature. By extrapolating the X-intercepts of the linear region in the M–S plots, V_{FB} of electrodes composed of ALD anatase TiO_2 film and rutile TiO_2 nanorod array are determined to be 0.167 and 0.038 V vs RHE (Figure 6a). Consequently, once the anatase and rutile contact, electrons would migrate from the Fermi level of rutile to that of anatase until their Fermi levels are equal. The carrier density N_d can be calculated from the slope of the linear region of M–S plots; the smaller slope of anatase TiO_2 suggests higher carrier density. This means that the Fermi level for the anatase is closer to the conduction band than rutile TiO_2 , and thus the conduction band of rutile TiO_2 is still higher than that of anatase. On the basis of the measured V_{FB} , N_d , and E_g , the band edges of TiO_2

before and after contact are plotted in Figure 6b. Upon light illumination, photogenerated electron–hole pairs can be separated at the AR junction interface, and then the electrons transfer from the rutile to anatase and are collected by the FTO substrate, whereas holes accumulate at the rutile surface for water oxidation in the electrolyte. Therefore, the internal electric field formed at the junction interface is beneficial to the charge separation and transport, which can contribute to higher photocurrent for the FTO/anatase/rutile photoanodes.

Panels c and d of Figure 6 show the M–S curves of ARs with different thicknesses of anatase films. The flat band potentials shift negatively and the slopes become lower from 20AR to 5AR. Lower slopes indicate higher N_d , which can be calculated from the above M–S equation:

$$N_d = (2/\epsilon\epsilon_0)[d(1/C^2)/dV]^{-1}$$

The calculated N_d values of 5AR, 10AR, and 20AR are 5.39×10^{18} , 4.72×10^{18} , and 3.77×10^{18} , respectively. The higher N_d raises the Fermi level of heterojunctions toward their conduction band and thus decreases the V_{FB} . As a result, the onset potentials shift to more negative values with decreased thicknesses of anatase films (Figure 5b). It is noted that the V_{FB} of pristine TiO_2 is more negative than that of all the AR samples, whereas the onset potentials show the opposite results. In general, the onset potential is close to the V_{FB} of a semiconductor photoelectrode, but a large difference exists due to low O_2 evolution dynamics and recombination.^{40–42} Therefore, the more negative onset potentials in all AR samples also imply less carrier recombination than the pristine TiO_2 , which is consistent with the J – t results in Figure 5c. For the RA junctions, a completely opposite process occurs; that is, photogenerated holes will migrate to the interface between rutile nanorods and FTO substrates. Holes accumulated at the interfaces cannot transfer to the electrode surface for oxidation reaction and will recombine with photogenerated electrons at the conduction band of TiO_2 , leading to decreased photocurrent densities. Therefore, when the FTO/rutile/anatase TiO_2 are used as photoanodes, larger external potentials are necessary to overcome the internal potential, and thus the onset potentials shift positively in the RA heterostructures.

CONCLUSION

Two types of TiO_2 heterojunctions, i.e., anatase films/rutile nanorods and rutile nanorods/anatase films, are fabricated on FTO substrates as the PEC photoanode. The thickness of anatase TiO_2 films is controlled precisely from 5 to 20 nm by ALD. The XRD, Raman, and TEM characterizations confirm the presence of the heterojunctions. Through comparison of the PEC performance of AR and RA structures, the charge transfer direction across the junction is figured out. Photogenerated electrons tend to transfer from the rutile nanorods to anatase films, and holes are eager to migrate from anatase to the rutile surface. As a consequence, introducing FTO/anatase film/rutile nanorod junctions not only increases the photocurrent density but also shifts the onset potential negatively. The FTO/rutile nanorod/anatase film junctions have significant negative impact on PEC activity. This clear charge transport scenario between the TiO_2 phase junctions provides an important guide for future heterojunction-based photoelectrode design. In the future, we can further enhance the photocurrent density by combining phase junctions with other visible-light-harvesting (CuIn_2S_4 and CdS) semiconductors.

EXPERIMENTAL SECTION

Synthesis of Rutile/Anatase TiO_2 Mixed Junctions. The rutile/anatase TiO_2 mixed junctions were prepared by a two-step process. In the first step, a facile hydrothermal method was used to synthesize rutile TiO_2 nanorod arrays. Precursor solution consisted of 0.269 g of anhydrous citric acid, 1 mL of tetrabutyl titanate, 30 mL of concentrated hydrochloric acid (36–38% by weight), and 30 mL of deionized water. Cleaned FTO substrate was immersed in the precursor of a Teflon-lined stainless steel autoclave with the conductive side downward. The autoclave was heated to 150 °C for 6 h and naturally cooled to room temperature. After the reaction process, the samples were rinsed with deionized water and annealed in air at 500 °C for 2 h, and rutile TiO_2 nanorod arrays were obtained. In the second step, the ALD (Ensure NanoTech, Beijing, China) technique was used to coat an anatase TiO_2 film on the surface of rutile TiO_2 nanorod arrays at 150 °C. Titanium and oxygen precursors were tetra(dimethylamino)titanium (TDMAT; Jiangsu Nata Optoelectronic Materials Co., Ltd., China) and pure water. The thickness was controlled by the number of ALD cycles with a deposition rate of 0.50 Å per cycle. Finally, the samples were treated in air at 500 °C for 2 h, and the rutile/anatase TiO_2 mixed junctions were obtained.

Synthesis of Anatase/Rutile TiO_2 Mixed Junctions. The anatase/rutile TiO_2 mixed junctions were prepared according to a similar method as mentioned above. First, the anatase TiO_2 films were deposited on cleaned FTO substrates in the ALD system. Then the rutile TiO_2 nanorod arrays were grown on the ALD treated substrates by the hydrothermal method and annealed in air at 500 °C for 2 h, and the anatase/rutile TiO_2 mixed junctions were prepared.

Materials Characterization. The morphologies of the synthesized samples were characterized by a field emission scanning electron microscope (FESEM; Hitachi SU8010, Japan). The microstructure was analyzed by TEM and HRTEM (FEI Tecnai G20 S-TWIN TMP, FEI, USA). The phase was measured by XRD. The absorption and reflectance spectra were collected by a UV–vis spectrophotometer (Shimadzu UV-3600, Japan).

Photoelectrochemical Measurements. Photoelectrochemical measurements were carried out in the electrolyte containing 0.1 M KOH (pH ~13) under a three-electrode system on an electrochemical workstation (PGSTAT 302N, Autolab). The work electrodes were the as-prepared rutile TiO_2 , FTO/rutile/anatase TiO_2 , and FTO/anatase/rutile TiO_2 samples, the counter electrode was a Pt mesh, and the reference electrode was a saturated Ag/AgCl electrode. During the measurement, the inert gas N_2 was used to remove the dissolved oxygen in the electrolyte. The current density versus potential and time curves with light on/off cycle measurements were performed in the above system under simulated solar illumination (100 mW cm^{-2}) provided by a solar light simulator (Newport, 94043A, USA). The curves were recorded by scanning the potential from the negative to the positive direction with a scan rate of 0.01 V s^{-1} . Mott–Schottky plots were obtained by the same workstation at an AC frequency of 1.0 kHz with an amplitude of 0.01 V in the dark.

ASSOCIATED CONTENT

Supporting Information

The Supporting Information is available free of charge on the ACS Publications website at DOI: 10.1021/acsami.6b03842.

Top and cross-sectional SEM images of AR and RA samples, XRD pattern of AR samples, Raman spectrum of rutile TiO_2 , TEM images of RAs, absorption curves of TiO_2 , and long-term J – t curves of AR and RA samples (PDF)

AUTHOR INFORMATION

Corresponding Authors

*(X.W.) E-mail: xudong.wang@wisc.edu.

*(L.L.) E-mail: lli@suda.edu.cn.

Author Contributions

[†]F.C. and J.X. contributed equally to this work.

Notes

The authors declare no competing financial interest.

ACKNOWLEDGMENTS

We acknowledge support from the National Natural Science Foundation of China (51422206, 51372159), 1000 Youth Talents Plan, Jiangsu Shuangchuang Plan, Distinguished Young Scholars Foundation by Jiangsu Science and Technology Committee (BK20140009), National 973 Basic Research Program of China (2015CB358600), and Priority Academic Program Development of Jiangsu Higher Education Institutions (PAPD).

REFERENCES

- (1) Tian, J.; Zhao, Z.; Kumar, A.; Boughton, R. I.; Liu, H. Recent Progress in Design, Synthesis, and Applications of One-dimensional TiO₂ Nanostructured Surface Heterostructures: A Review. *Chem. Soc. Rev.* **2014**, *43*, 6920–6937.
- (2) Yin, X.; Shi, J.; Niu, X.; Huang, H.; Wang, X. Wedding Cake Growth Mechanism in One-Dimensional and Two-Dimensional Nanostructure Evolution. *Nano Lett.* **2015**, *15*, 7766–7772.
- (3) Jia, L.; Bogdanoff, P.; Ramírez, A.; Bloeck, U.; Stellmach, D.; Fiechter, S. Fe₂O₃ Porous Film with Single Grain Layer for Photoelectrochemical Water Oxidation: Reducing of Grain Boundary Effect. *Adv. Mater. Interfaces* **2016**, *3*, 1500434.
- (4) Walter, M. G.; Warren, E. L.; McKone, J. R.; Boettcher, S. W.; Mi, Q.; Santori, E. A.; Lewis, N. S. Solar Water Splitting Cells. *Chem. Rev.* **2010**, *110*, 6446–6473.
- (5) Chen, X.; Shen, S.; Guo, L.; Mao, S. S. Semiconductor-based Photocatalytic Hydrogen Generation. *Chem. Rev.* **2010**, *110*, 6503–6570.
- (6) Wang, T.; Luo, Z.; Li, C.; Gong, J. Controllable Fabrication of Nanostructured Materials for Photoelectrochemical Water Splitting via Atomic Layer Deposition. *Chem. Soc. Rev.* **2014**, *43*, 7469–7484.
- (7) Iwashina, K.; Iwase, A.; Ng, Y. H.; Amal, R.; Kudo, A. Z-Schematic Water Splitting into H₂ and O₂ Using Metal Sulfide as a Hydrogen-Evolving Photocatalyst and Reduced Graphene Oxide as a Solid-State Electron Mediator. *J. Am. Chem. Soc.* **2015**, *137*, 604–607.
- (8) Ai, G.; Li, H.; Liu, S.; Mo, R.; Zhong, J. Solar Water Splitting by TiO₂/CdS/Co–Pi Nanowire Array Photoanode Enhanced with Co–Pi as Hole Transfer Relay and CdS as Light Absorber. *Adv. Funct. Mater.* **2015**, *25*, 5706–5713.
- (9) Li, X.; Yu, J.; Low, J.; Fang, Y.; Xiao, J.; Chen, X. Engineering Heterogeneous Semiconductors for Solar Water Splitting. *J. Mater. Chem. A* **2015**, *3*, 2485–2534.
- (10) Liu, S.; Liao, Q.; Lu, S.; Zhang, Z.; Zhang, G.; Zhang, Y. Strain Modulation in Graphene/ZnO Nanorod Film Schottky Junction for Enhanced Photosensing Performance. *Adv. Funct. Mater.* **2016**, *26*, 1347–1353.
- (11) Zhang, Z.; Liao, Q. L.; Yu, Y. H.; Wang, X. D.; Zhang, Y. Enhanced Photoresponse of ZnO Nanorods-Based Self-Powered Photodetector by Piezotronic Interface Engineering. *Nano Energy* **2014**, *9*, 237–244.
- (12) Zhang, Y.; Yan, X. Q.; Yang, Y.; Huang, Y. H.; Liao, Q. L.; Qi, J. Scanning Probe Study on the Piezotronic Effect in ZnO Nanomaterials and Nanodevices. *Adv. Mater.* **2012**, *24*, 4647–4655.
- (13) Zhang, J.; Xu, Q.; Feng, Z.; Li, M.; Li, C. Importance of the Relationship between Surface Phases and Photocatalytic Activity of TiO₂. *Angew. Chem.* **2008**, *120*, 1790–1793.
- (14) Wang, X.; Xu, Q.; Li, M.; Shen, S.; Wang, X.; Wang, Y.; Feng, Z.; Shi, J.; Han, H.; Li, C. Photocatalytic Overall Water Splitting Promoted by an α – β phase Junction on Ga₂O₃. *Angew. Chem., Int. Ed.* **2012**, *51*, 13089–13092.
- (15) Zhu, Y.; Liu, Y.; Lv, Y.; Ling, Q.; Liu, D.; Zhu, Y. Enhancement of Photocatalytic Activity for BiPO₄ via Phase Junction. *J. Mater. Chem. A* **2014**, *2*, 13041–13048.
- (16) Fang, Z.; Weng, S.; Ye, X.; Feng, W.; Zheng, Z.; Lu, M.; Lin, S.; Fu, X.; Liu, P. Defect Engineering and Phase Junction Architecture of Wide-Bandgap ZnS for Conflicting Visible Light Activity in Photocatalytic H₂ Evolution. *ACS Appl. Mater. Interfaces* **2015**, *7*, 13915–13924.
- (17) Yan, P.; Wang, X.; Zheng, X.; Li, R.; Han, J.; Shi, J.; Li, A.; Gan, Y.; Li, C. Photovoltaic Device based on TiO₂ Rutile/Anatase Phase Junctions Fabricated in Coaxial Nanorod Arrays. *Nano Energy* **2015**, *15*, 406–412.
- (18) Fujishima, A.; Honda, K. Electrochemical Photolysis of Water at a Semiconductor Electrode. *Nature* **1972**, *238*, 37–38.
- (19) Sun, X.; Dai, W.; Wu, G.; Li, L.; Guan, N.; Hunger, M. Evidence of Rutile-to-Anatase Photo-Induced Electron Transfer in Mixed-Phase TiO₂ by Solid-State NMR Spectroscopy. *Chem. Commun.* **2015**, *51*, 13779–13782.
- (20) Cai, J.; Wang, Y.; Zhu, Y.; Wu, M.; Zhang, H.; Li, X.; Jiang, Z.; Meng, M. In Situ Formation of Disorder-Engineered TiO₂(B)-Anatase Heterophase Junction for Enhanced Photocatalytic Hydrogen Evolution. *ACS Appl. Mater. Interfaces* **2015**, *7*, 24987–24992.
- (21) Mi, Y.; Weng, Y. Band Alignment and Controllable Electron Migration between Rutile and Anatase TiO₂. *Sci. Rep.* **2015**, *5*, 11482.
- (22) Zhang, D.; Yang, M.; Dong, S. Electric-Dipole Effect of Defects on the Energy Band Alignment of Rutile and Anatase TiO₂. *Phys. Chem. Chem. Phys.* **2015**, *17*, 29079–29084.
- (23) Smith, W. A.; Sharp, I. D.; Strandwitz, N. C.; Bisquert, J. Interfacial Band-Edge Energetics for Solar Fuels Production. *Energy Environ. Sci.* **2015**, *8*, 2851–2862.
- (24) Zhou, P.; Yu, J.; Jaroniec, M. All-Solid-State Z-Scheme Photocatalytic Systems. *Adv. Mater.* **2014**, *26*, 4920–4935.
- (25) Wang, X.; Jin, S.; An, H.; Wang, X.; Feng, Z.; Li, C. Relation between the Photocatalytic and Photoelectrocatalytic Performance for the Particulate Semiconductor-Based Photoconversion Systems with Surface Phase Junction Structure. *J. Phys. Chem. C* **2015**, *119*, 22460–22464.
- (26) Hwang, Y. J.; Hahn, C.; Liu, B.; Yang, P. Photoelectrochemical Properties of TiO₂ Nanowire Arrays: A Study of the Dependence on Length and Atomic Layer Deposition Coating. *ACS Nano* **2012**, *6*, 5060–5069.
- (27) Wang, G.; Wang, H.; Ling, Y.; Tang, Y.; Yang, X.; Fitzmorris, R. C.; Wang, C.; Zhang, J. Z.; Li, Y. Hydrogen-Treated TiO₂ Nanowire Arrays for Photoelectrochemical Water Splitting. *Nano Lett.* **2011**, *11*, 3026–3033.
- (28) Li, Y.; Takata, T.; Cha, D.; Takanabe, K.; Minegishi, T.; Kubota, J.; Domen, K. Vertically Aligned Ta₃N₅ Nanorod Arrays for Solar-Driven Photoelectrochemical Water Splitting. *Adv. Mater.* **2013**, *25*, 125–131.
- (29) Xu, M.; Da, P.; Wu, H.; Zhao, D.; Zheng, G. Controlled Sn-doping in TiO₂ Nanowire Photoanodes with Enhanced Photoelectrochemical Conversion. *Nano Lett.* **2012**, *12*, 1503–1508.
- (30) Ai, G.; Li, H.; Liu, S.; Mo, R.; Zhong, J. Solar Water Splitting by TiO₂/CdS/Co–Pi Nanowire Array Photoanode Enhanced with Co–Pi as Hole Transfer Relay and CdS as Light Absorber. *Adv. Funct. Mater.* **2015**, *25*, 5706–5713.
- (31) Grätzel, M. Photoelectrochemical Cells. *Nature* **2001**, *414*, 338–344.
- (32) Yu, Q.; Meng, X.; Wang, T.; Li, P.; Ye, J. Hematite Films Decorated with Nanostructured Ferric Oxyhydroxide as Photoanodes for Efficient and Stable Photoelectrochemical Water Splitting. *Adv. Funct. Mater.* **2015**, *25*, 2686–2692.
- (33) Li, C.; Zhu, X.; Zhang, H.; Zhu, Z.; Liu, B.; Cheng, C. 3D ZnO/Au/CdS Sandwich Structured Inverse Opal as Photoelectrochemical Anode with Improved Performance. *Adv. Mater. Interfaces* **2015**, *2*, 1500428.
- (34) Guo, X.; Wang, L.; Tan, Y. Hematite Nanorods Co-doped with Ru Cations with Different Valence States as High Performance Photoanodes for Water Splitting. *Nano Energy* **2015**, *16*, 320–328.

- (35) Wolcott, A.; Smith, W. A.; Kuykendall, T. R.; Zhao, Y.; Zhang, J. Z. Photoelectrochemical Water Splitting using Dense and Aligned TiO₂ Nanorod Arrays. *Small* **2009**, *5*, 104–111.
- (36) Hahn, N. T.; Mullins, C. B. Photoelectrochemical Performance of Nanostructured Ti- and Sn-doped α -Fe₂O₃ Photoanodes. *Chem. Mater.* **2010**, *22*, 6474–6482.
- (37) Klahr, B.; Gimenez, S.; Fabregat-Santiago, F.; Bisquert, J.; Hamann, T. W. Photoelectrochemical and Impedance Spectroscopic Investigation of Water Oxidation with “Co–Pi”-Coated Hematite Electrodes. *J. Am. Chem. Soc.* **2012**, *134*, 16693–16700.
- (38) Moniz, S. J. A.; Zhu, J.; Tang, J. 1D Co-Pi Modified BiVO₄/ZnO Junction Cascade for Efficient Photoelectrochemical Water Cleavage. *Adv. Energy Mater.* **2014**, *4*, 1301590.
- (39) Wang, C.; Chen, Z.; Jin, H.; Cao, C.; Li, J.; Mi, Z. Enhancing Visible-Light Photoelectrochemical Water Splitting Through Transition-Metal Doped TiO₂ Nanorod Arrays. *J. Mater. Chem. A* **2014**, *2*, 17820–17827.
- (40) Iandolo, B.; Zhang, H.; Wickman, B.; Zorić, I.; Conibeerb, G.; Hellman, A. Correlating Flat Band and Onset Potentials for Solar Water Splitting on Model Hematite Photoanodes. *RSC Adv.* **2015**, *5*, 61021–61030.
- (41) Shinde, P. S.; Choi, S. H.; Kim, Y.; Ryu, J.; Jang, J. S. Onset Potential Behavior in α -Fe₂O₃ Photoanodes: The Influence of Surface and Diffusion Sn Doping on the Surface States. *Phys. Chem. Chem. Phys.* **2016**, *18*, 2495–2509.
- (42) Cao, D.; Luo, W.; Feng, J.; Zhao, X.; Li, Z.; Zou, Z. Cathodic Shift of Onset Potential for Water Oxidation on a Ti⁴⁺ Doped Fe₂O₃ Photoanode by Suppressing the Back Reaction. *Energy Environ. Sci.* **2014**, *7*, 752–759.